Carbon 243 (2025) 120561

Contents lists available at ScienceDirect

Carbon

journal homepage: www.elsevier.com/locate/carbon

Flash Joule heating-enhanced in-situ synthesis of 3D graphene/high-entropy alloy composites for efficient electromagnetic wave absorption

Wen Fan [a,1], Zhao Li [b,c,1], Jixiang Zhang [a,*], Yanping Song [b,d], Shudong Zhang [b,d], Cui Liu [b,d], Shuai Han [b,f], Yi Dong [a], Zheng Xu [a], Na Hong [b,c], Jun Kang [b,c], Shihao Wang [b,c], Zhiyuan Yang [e], Nian Li [b,d,**], Zhenyang Wang [b,d,***]

[a] School of the Chongqing Jiaotong University, Chongqing, 400074, China
[b] Institute of Solid-State Physics, Chinese Academy of Science, Hefei, Anhui, 230031, China
[c] Department of Chemistry, University of Science and Technology of China, Hefei, Anhui, 230026, China
[d] Key Laboratory of Photovoltaic and Energy Conservation Materials, Hefei Institutes of Physical Science, Chinese Academy of Sciences, Hefei, 230031, China
[e] School of Energy Materials & Chemical Engineering, Hefei University, Hefei, Anhui, 230601, China
[f] School of Mathematics and Physics, Hebei University of Engineering, Handan, 056038, Hebei, China

ARTICLE INFO

Keywords:
High-entropy alloy composites
Flash Joule heating synthesis
3D graphene matrix
Electromagnetic wave absorption
Synergistic effects in HEAs

ABSTRACT

High-entropy alloys (HEAs) have emerged as a promising class of materials for electromagnetic wave absorption (EWA) due to their unique electronic structures and the synergistic effects of multiple components. However, the practical application of HEAs has been limited by their narrow Effective Absorption Bandwidth (EABw) and high density. Herein, the in-situ synthesis of 3D graphene/HEA composites via a novel method combining laser-induced synthesis and flash Joule heating (FJH) technology is reported. The unique 3D porous structure of graphene provides a lightweight and conductive matrix for the uniform distribution of HEA nanoparticles. The FJH treatment not only ensures the intimate contact between the graphene matrix and HEA nanoparticles but also refines the grain size of the alloy and optimizes the FeCoNiCuMn HEA composition. The resulting 3D graphene/HEA composites demonstrated exceptional EWA performance, achieving a minimum reflection loss of −62.23 dB at 2–18 GHz with a filler ratio of 20 wt% in paraffin wax. Moreover, the EABw reached 5.05 GHz with a filler ratio of 30 wt%. These findings highlight the potential of 3D graphene/HEA composites synthesized via laser-induction and FJH methods for developing advanced EWA materials with broad applications in electromagnetic compatibility, stealth technology, and communication systems.

1. Introduction

With the rapid progress of modern technology, electromagnetic waves are essential in communication, radar, and electronics [1]. However, their extensive use has led to issues like interference, health risks from radiation, and equipment performance degradation [2]. The development of electromagnetic wave-absorbing (EWA) materials is crucial as they absorb and dissipate electromagnetic energy, reducing interference and radiation hazards to ensure equipment functionality and human health [3].

Currently, EWA materials such as ferrites, carbon materials, and conductive polymers are widely used [4]. However, they have inherent limitations [5]. Ferrites, despite their good magnetic loss properties, are too dense for lightweight applications [6]. Carbon materials, though lightweight and conductive, have a narrow absorption bandwidth, limiting wideband absorption [7–9]. Furthermore, materials with a single absorption mechanism struggle to meet the demands for high performance, lightweight, and wide bandwidth simultaneously,

* Corresponding author.
** Corresponding author. Institute of Solid-State Physics, Chinese Academy of Science, Hefei, Anhui, 230031, China.
*** Corresponding author. Institute of Solid-State Physics, Chinese Academy of Science, Hefei, Anhui, 230031, China.
E-mail addresses: jixiangzhang@163.com (J. Zhang), linian@issp.ac.cn (N. Li), zywang@iim.ac.cn (Z. Wang).
[1] These authors contribute equally.

https://doi.org/10.1016/j.carbon.2025.120561
Received 13 April 2025; Received in revised form 5 June 2025; Accepted 20 June 2025
Available online 20 June 2025

restricting their practical effectiveness [10].

High-entropy alloys (HEAs), as a novel type of alloy material, have shown great potential in the field of EWA due to several unique properties [11–13]. The high entropy effect in thermodynamics stabilizes the alloy structure, preventing phase separation and promoting a uniform solid solution, which, by optimizing interfacial polarization in these atomic-scale composites, enhances the material's EWA performance [14–16]. Additionally, the lattice distortion effect disrupts the regular arrangement of atoms, increasing the material's resistance to electron flow and contributing to higher dielectric loss [17–19]. Further, the degree of lattice distortion can effectively control the magnetic properties of the material [20]. The hysteretic diffusion effect creates dipoles via atomic pairs and defects at different frequencies, and distorted sites scatter electrons, boosting dielectric loss and absorption bandwidth [21–23]. The cocktail effect results from the synergistic interaction of multiple elements, each contributing to the overall absorption performance [24]. However, HEAs also face challenges such as difficulties in fabrication, insufficient performance optimization, and their relatively high density, which limits their application in lightweight materials [25]. These factors currently hinder their widespread practical application.

To address the limitations of HEAs, the development of carbon-based composite materials offers significant advantages. Carbon materials [26], with their lightweight nature and excellent electrical properties, can effectively reduce the overall density of the composite while enhancing its electromagnetic performance. Graphene [27], in particular, stands out due to its exceptional electrical conductivity, high specific surface area, and superior mechanical strength, making it an ideal candidate for improving the EWA capabilities of composite materials. Consequently, graphene/HEA composites have garnered considerable attention in the field of EWA. For instance, core-shell HEA@C-NPs nanocapsules synthesized via an arc discharge plasma method achieved a minimum reflection loss of −33.4 dB at 3.34 mm and an EAB of 5.45 GHz at 1.9 mm [28]. Composites formed by dispersing $(MnNiCuZn)_{0.7}Co_{0.3}Fe_2O_4$ on graphene flakes via a solution combustion method achieved a minimum reflection loss of −27 dB at 5.3 mm [29]. The high conductivity of graphene flakes contributed to high dielectric loss, enhancing the EWA properties of the composites. These examples demonstrate that the integration of carbon-based materials and HEAs overcome the limitations of single-material systems, enhancing composite microwave absorption through multiple attenuation mechanisms.

However, there are still challenges to be addressed, such as the weak interfacial bonding between HEAs and the graphene matrix [30], which can affect the overall performance and stability of the composite. Additionally, achieving a uniform distribution of HEAs within the composite remains a technical hurdle. Addressing these issues through advanced fabrication techniques will be crucial for maximizing the potential of graphene/HEA composites in EWA applications.

In this study, by combining laser-induced graphene (LIG) technology with flash Joule heating (FJH) technology, the in-situ synthesis of FeCoNiCuMn high-entropy alloy nanocrystals on the surface of 3D porous graphene has been successfully achieved. The LIG technology utilizes laser irradiation of polyimide films to rapidly carbonize and form a 3D porous graphene structure, providing a lightweight, conductive, and high-specific-surface-area matrix for the HEA nanocrystals. This ensures the uniform distribution of the alloy nanocrystals and offers abundant interfaces for multiple reflections and scattering of electromagnetic waves. The FJH technology, through instantaneous high-temperature treatment, produces more uniform and finer HEA nanocrystals. Such grain refinement effect is demonstrated to enhance the magnetic and dielectric properties of the alloy, thereby improving the EWA capability of the composite material. Furthermore, the structure of the composite material has been meticulously optimized by precisely adjusting the composition and proportion of the HEA, resulting in significantly improved EWA performance across a wide frequency band. At frequencies ranging from 2 to 18 GHz, the composite material exhibited a minimum reflection loss of −62.23 dB with a filler ratio of 20 wt% in paraffin wax. Additionally, the maximum effective absorption bandwidth reached 5.05 GHz with a filler ratio of 30 wt%. These results are attributed to the synergistic effects of high-entropy-induced lattice distortion, which optimizes impedance matching, and the enhanced magnetic and dielectric properties from the FeCoNi base alloy and the addition of Mn and Cu, ultimately improving the overall absorption performance. The composites are expected to play a significant role in areas such as military stealth technology, electromagnetic compatibility of electronic devices, and the enhancement of anti-interference performance in communication equipment.

2. Experimental section

2.1. Chemical reagents

N, N-dimethylacetamide (DMAc), Polyimide solution (PI, thermoplastic), and ferric chloride, cobalt chloride, nickel chloride, cupric chloride, and manganese chloride were purchased from Sinopharm Chemical Reagent Co., Ltd. (Shanghai, China). All chemical reagents were not further treated.

2.2. Synthesis of precursor PI films

The precursor PI films containing metal salts were prepared via a classical two-step method [31]. Initially, five metal salts ($FeCl_3{\cdot}6H_2O$, $CoCl_2{\cdot}6H_2O$, $NiCl_2{\cdot}6H_2O$, $CuCl_2{\cdot}2H_2O$, and $MnCl_2{\cdot}4H_2O$) were dissolved in N,N-dimethylacetamide (DMAc) to create FeCoNiCuMn solutions with a molar ratio of the five elements being 1:1:1:1:1. In addition, to investigate the effects of varying Cu and Mn contents, $FeCoNiCu_xMn_{1-x}$ solutions with x = 0.2, 0.4, 0.6, and 0.8 were also prepared for comparison. For brevity, the laser-induced graphene composites containing $FeCoNiCu_xMn_{1-x}$ high-entropy alloys (x = 0.2, 0.4, 0.6, 0.8) are hereafter referred to as LIG/HEA-1-Cu_x (x = 0.2, 0.4, 0.6, 0.8). These salt solutions had a concentration of 3 mmol, with additional 1 mmol and 5 mmol solutions prepared as control groups to explore the impact of solution concentration.

The resulting metal salt solutions were mixed with a poly (amic acid) solution at a volume ratio of 1:2.5 and stirred for 1 h to form a uniform metal-polyimide complex solution. This complex solution was then spin-coated onto a glass plate or petri dish and subjected to stepwise heating in an oven (60 °C/2h, 90 °C/2h, 120 °C/2h, 150 °C/2h, 180 °C/2h) to evaporate the solvent. Upon completion of the heating process, PI films containing Fe^{3+}, Co^{2+}, Ni^{2+}, Cu^{2+}, and Mn^{2+} were successfully formed.

2.3. Preparation of LIG/HEA composites

The PI films containing metal salts were placed on a vacuum adsorption platform and processed using a 10.6 μm CO_2 laser marking system (SK–F30, Shanghai Sanke Laser Technology Co., Ltd., China). The laser parameters were set as follows: scan rate of 90 mm/s, line spacing of 0.1 mm, spot size of 0.1 mm, laser power of 5.8 W, and frequency of 10 kHz. The laser treatment was performed twice under the same conditions. In the first laser induction, the surface of PI was converted into a 3D porous LIG structure [32], and metal oxides (MO) were grown in situ on the surface of this LIG, resulting in a product referred to as LIG/MO. In the second laser induction, the metal oxides (MO) were reduced to form HEA nanoparticles via a carbothermal reduction process, yielding a product labeled as LIG/HEA-1. Subsequently, the product LIG/HEA-1 was scraped into a powder and subjected to FJH at a temperature of 2500 ± 80 °C for 1 s using a millisecond-pulsed flash Joule heating reactor (FJH-2024APLUS) under vacuum conditions. This process ultimately yielded HEA nanoparticles with smaller particle sizes, and the resulting product was designated as LIG/HEA-2.

2.4. Characterization

The physical phase analysis was carried out by X-ray diffraction (PANalytical X′ Pert PRO with Cu Kα radiation); Scanning Electron Microscope (SEM) images were obtained on an FEI Sirion 200 field-emission scanning electron microscope. Transmission Electron Microscope (TEM) and High-Resolution Transmission (HRTEM) images were obtained using a JEM 2100F transmission electron microscopy. TEM powder samples were dropped on the copper mesh after bath sonication treatment; the magnetic properties of the powder samples were tested by a vibrating sample magnetometer (VSM,MPMS XL5, Quantum Design) with a magnetic field strength of −20000~20000 Oe at room temperature; the Raman spectra were obtained by DXR Smart Raman Spectrometer at a wavelength of 532 nm and power of 10 mW; The electrical conductivity of the samples was tested using a multifunctional digital four-probe tester (ST-2258C). For the conductivity measurements, the samples were pressed into dense pellets using a hydraulic press at a pressure of 40 MPa to ensure uniform contact and accurate measurement. The specific surface area was surveyed on a Tristar II 3020 M by the Brunauer-Emmett-Teller (BET) method. The relative complex permittivity (ε_r) and permeability (μ_r) were measured via CEYEAR 3672B Vector Network Analyzer (Ceyear Technologies Co., Ltd) in the frequency range of 2~18 GHz. For the measurements, LIG/HEA powder was mixed homogeneously with paraffin wax at various mass ratios and then pressed into concentric ring samples with an inner diameter of 3.00 mm, an outer diameter of 7.00 mm, and a thickness of 2.00 mm.

3. Results and discussion

Fig. 1 illustrates the synthesis process of LIG/HEA-2 composites along with the wave-absorbing mechanisms. Initially, equimolar metal salt solutions of the five HEA components were mixed with N, N-dimethylacetamide (DMAc) and then combined with a thermosetting polyimide solution at a volume ratio of 1:2.5. After magnetic stirring for 1 h, a uniform metal-polyimide complex was formed. This complex was poured into a 120 mm petri dish, covered with aluminum foil overnight to remove air bubbles, and subsequently dried in a vacuum oven to form metal-polyimide films. The resulting metal-polyimide films were scanned using a CO_2 laser cutting system (wavelength 10.6 μm, model SK-F30) at a scanning rate of 90 mm/s, with a laser power of 5.8 W and a line spacing of 0.1 mm. The laser treatment was performed twice under the same conditions to ensure the formation of LIG/HEA-2.

Analysis of the laser process parameters (Fig. S1–S2, Supporting Information) reveals that higher laser power or more laser-induction cycles significantly alter the 3D graphene structure, consequently affecting the composite's EWA performance. During the first laser induction, the PI film is firstly converted into a 3D porous LIG structure [33]. Meanwhile, due to the presence of oxygen in the reaction environment, metal oxides (MO) are simultaneously generated and loaded onto the surface of the 3D porous LIG [34]. The product obtained from the first laser induction is referred to as LIG/MO (Fig. S3). In the subsequent second laser induction process, the elevated temperature causes the metal oxides to release oxygen, while the 3D structure of graphene remains unchanged. As the laser beam energy is absorbed by graphene, electrons in the valence band are excited to the conduction band, thereby realizing and maintaining energy level inversion [35]. Hot electrons with sufficient energy are ejected from graphene to become free electrons, which promote the reduction of metal ions [36]. Due to the non-wetting behavior between the metals and graphene, liquid metal droplets tend to aggregate and coarsen larger at high temperatures, thereby minimizing their surface energy [37]. The resulting product is referred to as LIG/HEA-1.

However, the relatively large particle size may weaken the interfacial polarization effect, leading to a reduction in the EWA efficiency of the composite material [38]. To address these issues, the alloy nanoparticles were refined using FJH. This process was conducted in a millisecond-pulsed flash Joule heating reactor (FJH-2024APLUS) with a supply voltage of 220 V, a total power of 3500 W, and capacitive currents ranging from 0 to 600 A. The above LIG/HEA-1 composite powder after two times of laser induction was collected and placed into a quartz tube. The FJH system was then rapidly discharged for 1 s, heating the material instantaneously to 2500 °C ± 80 °C with a heating duration of 80 ms (Fig. S4). After cooling to room temperature, the LIG/HEA-2 composites with smaller nanoparticles were obtained. This transient high-temperature process induces rapid diffusion and recrystallization of atoms on the alloy surface, leading to the formation of fine and uniform grains. Such grain refinement may induce alterations in the electrical conductivity and imaginary part of the dielectric constant within the composite, thereby influencing the EWA performance. These effects will be further explored through experimental investigation in subsequent sections [39]. When grain refinement occurs, the uniform distribution of elements can promote the formation of ferromagnetic phases in the material, thereby increasing the saturation magnetization. Additionally, the process may release internal stresses, further optimizing the alignment of magnetic domains and enhancing the material's magnetic properties. Collectively these changes facilitate impedance matching with electromagnetic waves, thereby enhancing absorption efficiency [40].

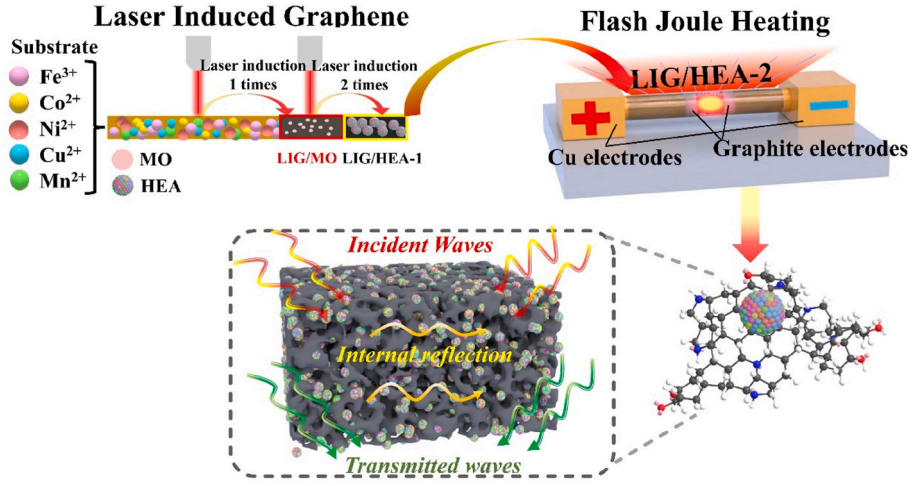

Fig. 1. Schematic illustration of the preparation process for LIG/HEA-2 composites via laser-induced synthesis and flash Joule heating, highlighting the formation of laser-induced graphene.

The selection of the alloying constituent elements was based on several considerations: Firstly, FeCoNi forms a standard alloy system known as the Cantor alloy [41]. Furthermore, the incorporation of copper is reported to enhance the alloy's strength, hardness, and corrosion resistance, while also improving its electrical conductivity, and also helping to reduce the coercivity of the material [42]. Meanwhile, manganese, frequently employed as a reinforcing element, contributes to the alloy's magnetic properties, hardness and strength [43]. This will be further explored in subsequent experimental studies.

The morphology and microstructure of the LIG/HEA composites were characterized using scanning electron microscopy (SEM) and transmission electron microscopy (TEM). As shown in Fig. 2a–f, spherical high-entropy alloy nanoparticles are attached to the surface of the 3D porous graphene. Notably, the particle sizes of the composites were initially large after laser induction, with sizes of approximately 60 nm, but were significantly reduced to about 20 nm following FJH, when the concentration of metal salt precursor solution was 1, 3, and 5 mmol. Additionally, the particles were more homogeneously distributed within the 3D porous graphene after FJH, which may significantly enhance EWA by improving electrical conductivity, impedance matching, and promoting multiple reflections and scattering within the material.

Fig. 2g–h presents the Energy Dispersive Spectroscopy (EDS) analysis of LIG/HEA-2 under the precursor concentration of 3 mmol. As can be seen, the metal elements Fe, Co, Ni, Cu, Mn are more uniformly distributed throughout the HEA nanoparticle. The elemental content measured is 18.6 at% of Fe, 23.8 at% of Co, 20.7 at% of Ni, 21.5 at% of Cu, and 15.4 at% of Mn. Fig. 2i presents high-resolution transmission electron microscopy (HR-TEM) images of the LIG/HEA-2 under the precursor concentration of 3 mmol, revealing lattice fringes with a spacing of 0.22 nm. This spacing corresponds to the (111) crystallographic plane of a face-centered cubic (FCC) structure, indicating the crystalline nature of the HEA nanoparticles. Selected-area electron diffraction (SAED) patterns, shown in Fig. 2j–k, further confirm the microstructures of the composites. These results indicate that the prepared nanoparticles are polycrystalline, a conclusion that will be further supported by XRD analysis.

To verify the phase structure of the LIG/HEA composites, XRD patterns are displayed in Fig. 3a and b. As shown in Fig. 3a for LIG/HEA-1

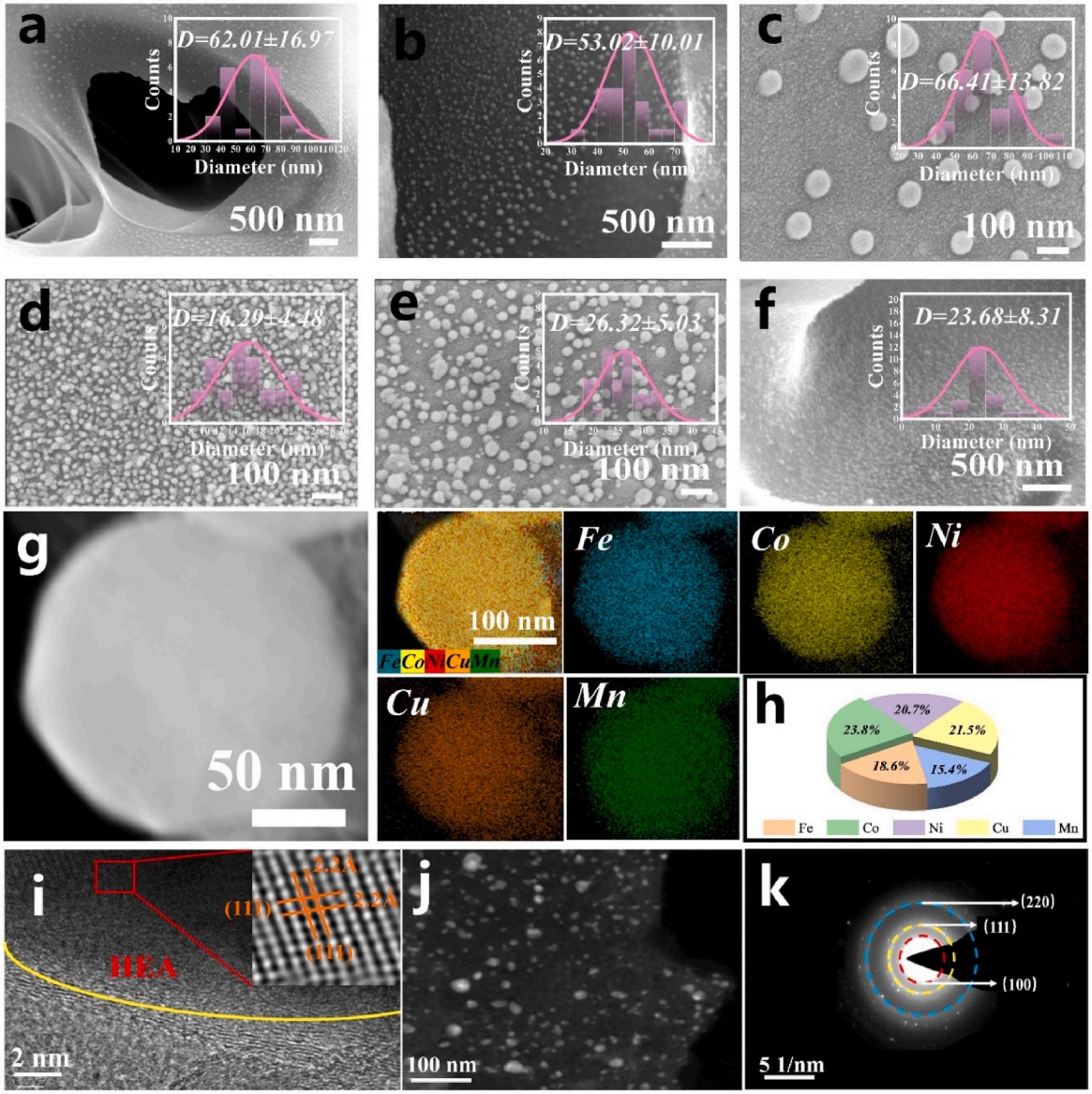

Fig. 2. Morphological and structural characterization of LIG/HEA-2 composites. (a–c) SEM images of LIG/HEA-1under the precursor concentration of 1、3、5 mmol; (d–f) SEM images of LIG/HEA-2 under the precursor concentration of 1、3、5 mmol; (g) EDS images, (h) elemental ratio, (i) HRTEM images, (j–k) SAED images of LIG/HEA-2 under the precursor concentration of 3 mmol.

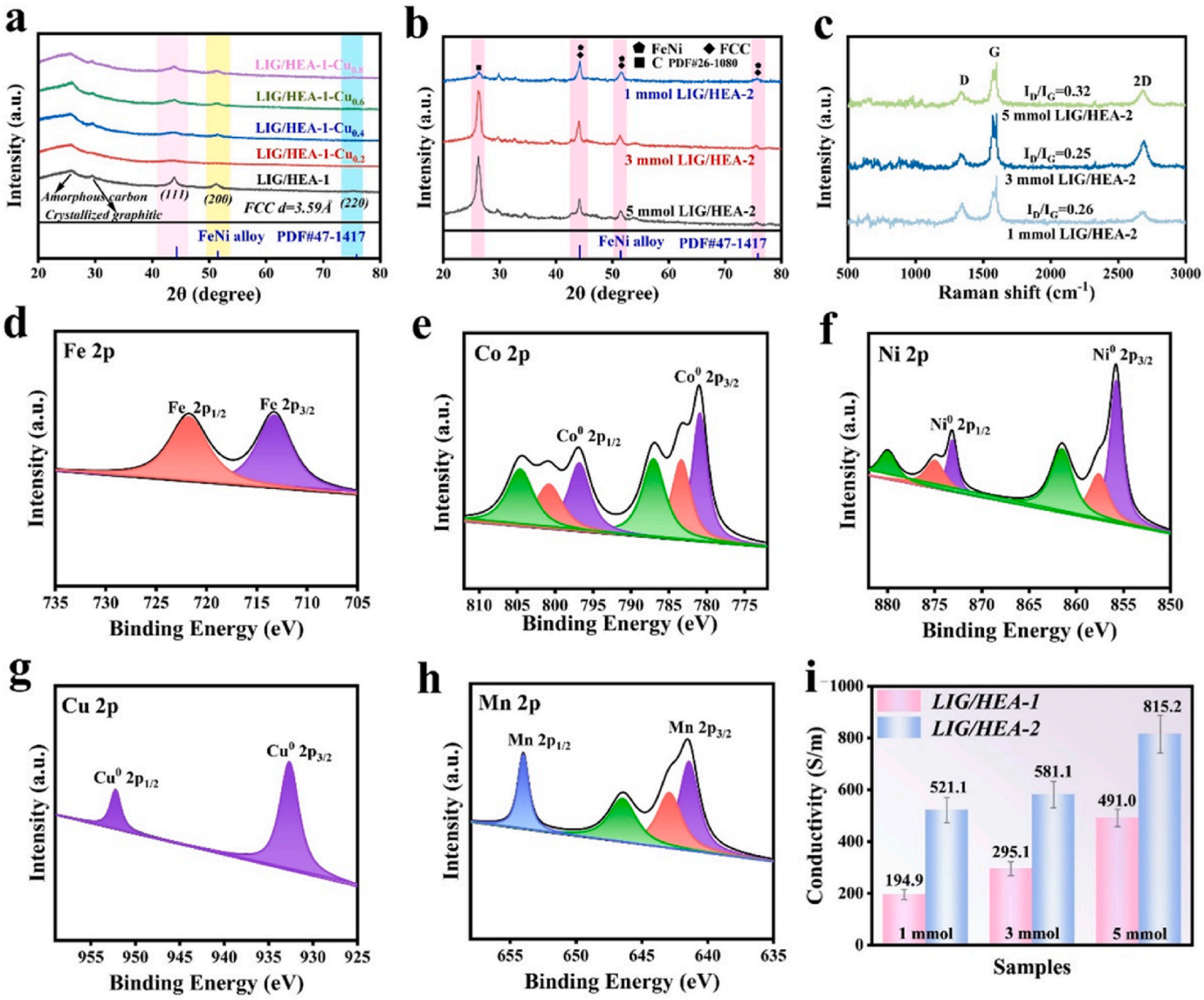

Fig. 3. Characterization of LIG/HEA composites. (a) XRD image of LIG/HEA-1 and LIG/HEA-1-Cu$_x$ (x = 0.2, 0.4, 0.6, 0.8); (b) XRD image of LIG/HEA-2; (c) Raman spectra of the LIG/HEA-2; (d–h) XPS of LIG/HEA-2; (i) Electrical conductivity analysis.

and LIG/HEA-1-Cu$_x$ (FeCoNiCu$_x$Mn$_{1-x}$, x = 0.2, 0.4, 0.6, 0.8), the FCC phase structure, dominated by the (111), (200), and (220) crystal planes, appears at diffraction angles of 44.21°, 51.52°, and 76.23°, respectively. These peaks correspond to the standard PDF#47–1417 positions and relative intensities, indicating that they can be identified as FeNi alloy, which dominates the alloy and forms larger grains. Co, Cu, and Mn are likely dissolved within the FeNi phase as a solid solution, leading to weaker diffraction peaks.

As shown in Fig. 3a, with the decrease of the molar ratio of Mn elements, the solid solubility of Mn in the alloy may decrease, leading to changes in the distribution of Mn atoms in the crystal lattice and a gradual decrease in the intensity of XRD peaks. When the molar ratio of the five metal elements is 1:1:1:1:1, the peaks in the XRD pattern are sharper and more intense, indicating the formation of a purer single phase with more uniform alloy composition and reduced phase separation. Therefore, the subsequent experiments were carried out with the molar ratio of FeCoNiCuMn being 1:1:1:1:1.

Comparing Fig. 3a and b, it can be seen that after FJH treatment, the carbon diffraction peaks at 26.22° and 29.12° become narrower and higher, indicating that the FJH process promotes the crystallization of amorphous carbon into a more ordered graphite structure. Comparing different precursor salt solution concentrations in Fig. 3b, when the concentration is 3 mmol, the intensity of the FeNi phase diffraction peak is the highest, indicating that this concentration is favorable for forming a uniform crystal structure and stable alloy phase. Both low and high concentrations of precursor salt solution can affect crystal nucleation and growth, resulting in a decrease in diffraction peak intensity.

To further substantiate the successful synthesis of the high-entropy alloy phase and elucidate the role of the FJH environment, supplementary XRD analyses were performed under varying conditions (Fig. S5). These analyses provide evidence: Fig. S5a demonstrates that calcination of the precursor in air leads to the formation of oxide phases (predominantly $CuMn_2O_4$), whereas the FJH process conducted under vacuum (as evidenced by Fig. 3a and b) effectively suppresses oxidation, yielding a pure FCC phase characteristic of the HEA. Furthermore, Fig. S5b confirms that the FCC peaks in our FJH-synthesized LIG/HEA composites align closely with those of a conventionally prepared FeCoNiCuMn alloy (high-temperature melting under argon atmosphere) of identical nominal composition. This close agreement validates that the FJH process successfully produces a stable high-entropy solid solution.

Fig. 3c presents the Raman spectra of LIG/HEA-2 under different

precursor solution concentrations. As can be seen, all the samples exhibit three characteristic peaks near 1345 cm^{-1}, 1586 cm^{-1}, and 2660 cm^{-1}, which correspond to the D, G, and 2D peaks of graphene, respectively, confirming the presence of graphene. Fig. S5 shows the Raman spectra of LIG/HEA-1 composites. In comparison, the ratio of the D peak to the G peak of LIG/HEA-2 (0.25–0.32) is smaller than that of LIG/HEA-1 (0.42–0.52), indicating that LIG/HEA-2 has a higher crystalline quality.

The electronic states of the elements on the surface of LIG/HEA-2 under the precursor concentration of 3 mmol were analyzed using X-ray photoelectron spectroscopy (XPS). The XPS spectra of Fe, Co, Ni, Cu, and Mn in the 2p orbitals are shown in Fig. 3d–h, respectively. In the Fe 2p XPS spectra, the 712.7 and 724.2 eV peaks are attributed to Fe^{2+} $2p_{3/2}$ and Fe^{3+} $2p_{1/2}$, respectively. In the Co 2p XPS spectra, the 778.6 and 793.3 eV peaks correspond to Co^0, and the peaks at 781.3 and 786.5 eV are attributed to the Co^{3+} $2p_{3/2}$ and Co^{2+} $2p_{1/2}$. Similarly, Ni^0, Ni^{2+}, and Ni^{3+} peaks are observed in the Ni 2p XPS spectra, while the peaks at 856.2 eV and 872.3 eV can be attributed to Ni^0. As for the Cu 2p spectra, the peaks at 932.8 eV and 952.8 eV can be attributed to Cu^0. In the fine XPS spectra of Mn 2p, Mn^{2+} $2p_{3/2}$ corresponds to 641.5 eV, and Mn^{4+} $2p_{1/2}$ corresponds to 654.6 eV, and there is no prominent Mn^0 peak [44]. These results reveal the coexistence of metallic and oxidized states in the metallic elements. The metallic state reflects the inherent characteristics of HEAs, while the oxidized state likely originates from partial oxidation due to the high surface energy of the nanoparticles.

Fig. 3i illustrates the electrical conductivity of the composites. It is observed that the electrical conductivity of the LIG/HEA-2 is higher than that of the LIG/HEA-1 composites. Specifically, the electrical conductivity of the LIG/HEA-1 composites increases from 194.9 S/m to 491.0 S/m, and that of the LIG/HEA-2 composites increases from 521.1 S/m to 815.2 S/m as the concentration of precursor salt solution increases from 1 mmol to 5 mmol. These results further demonstrate that the FJH process effectively repairs defects in graphene and forms a high-quality sp^2 carbon network, thereby enhancing electrical conductivity [45]. Notably, controlled synthesis of LIG/HEA composites revealed that reducing HEA grain size (26.32 ± 5.03 nm vs. 53.02 ± 10.01 nm) unexpectedly enhances electrical conductivity through synergistic mechanisms: increased interfacial area strengthens M − C covalent bonding for efficient electron transfer, while finer particle dispersion forms higher-density conductive networks. This enhanced conductivity implies an increased concentration of free electrons, thereby boosting conductive loss and ultimately improving the material's electromagnetic wave absorption capability.

The specific surface area and pore structure of the LIG/HEA under precursor concentration of 3 mmol were characterized using nitrogen adsorption-desorption curves. As indicated by the effective medium theory [46], the porous structure is likely to reduce the dielectric constant of the medium and enhance its impedance-matching properties. Fig. S6 shows the typical Type I and Type IV curves when the relative pressure (P/P_0) exceeds 0.9. Due to the 3D porous structure of graphene, the specific surface area and pore volume of LIG/HEA-1 composites are 31.98 $m^2\ g^{-1}$ and 0.09 $cm^3\ g^{-1}$, respectively, while those of LIG/HEA-2 composites are 56.78 $m^2\ g^{-1}$ and 0.11 $cm^3\ g^{-1}$. After FJH, the specific surface area and pore structure of LIG/HEA-2 gradually increase, which may be due to the small-sized grains. Moreover, distinct hysteresis loops are observed for both LIG/HEA-1 and LIG/HEA-2 in the relative pressure range of 0.55–0.99, indicating the presence of micro and mesopores [47].

As is well known, magnetic properties play a crucial role in the EWA capability. Therefore, the magnetic properties of the materials were characterized and analyzed. Fig. 4a and b shows the hysteresis loops of the LIG/HEA-1and LIG/HEA-1-Cu_x (x = 0.2, 0.4, 0.6, 0.8) composites under precursor solution concentration of 3 mmol. FeCoNi, being typical ferromagnetic elements, exhibits superior soft magnetic properties characterized by a high saturation magnetization (M_s) of 4.9 emu/g and a low coercivity (Hc) of 40 Oe under low-field conditions (Fig. 4a and b). When Cu, a non-magnetic element, is added to the FeCoNi base alloy, it dilutes the concentration of magnetic elements, leading to a decrease in M_s. As shown in Fig. 4a, the M_s of FeCoNiCu is 1.4 emu/g, a significant

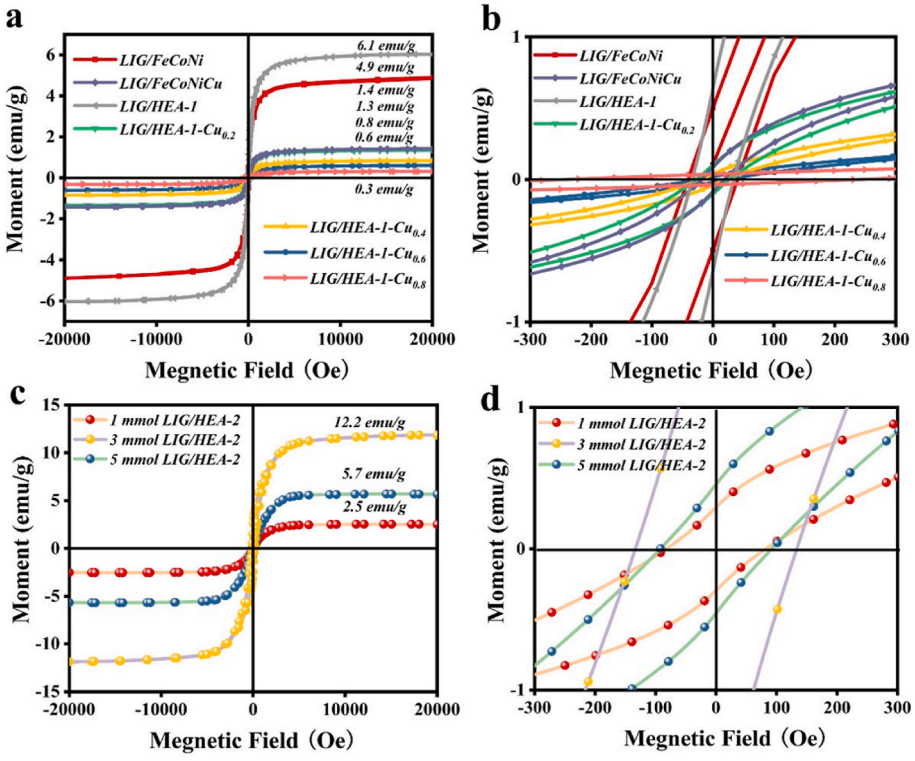

Fig. 4. Hysteresis loop analysis of the composites. (a–b) Hysteresis loops of LIG/HEA-1 under precursor concentration of 3 mmol and low-field conditions; (c–d) Hysteresis loops of LIG/HEA-2 and low-field conditions.

reduction compared to FeCoNi, while the Hc value is significantly reduced to 22 Oe, indicating that Cu primarily affects the magnetization strength with a notable impact on coercivity. Low coercivity means that the material can more quickly return to a non-magnetic state after the external magnetic field is removed, and thereby enhances the material's EWA efficiency [48].

Introducing Mn to FeCoNiCu further complicates the magnetic behavior. Mn exhibits complex magnetic properties, showing ferromagnetic behavior at low concentrations but potentially forming antiferromagnetic or paramagnetic phases at higher concentrations [49]. Fig. 4a and b shows that LIG/HEA-1 has a M_s of 6.1 emu/g and a Hc of 34 Oe. Compared to FeCoNi, the M_s is significantly enhanced, while the coercivity is reduced. This suggests that Mn may compensate for the magnetic dilution effect of Cu, maintaining a high M_s while reducing defects and secondary phases that hinder magnetic domain wall movement, thus lowering the Hc [50].

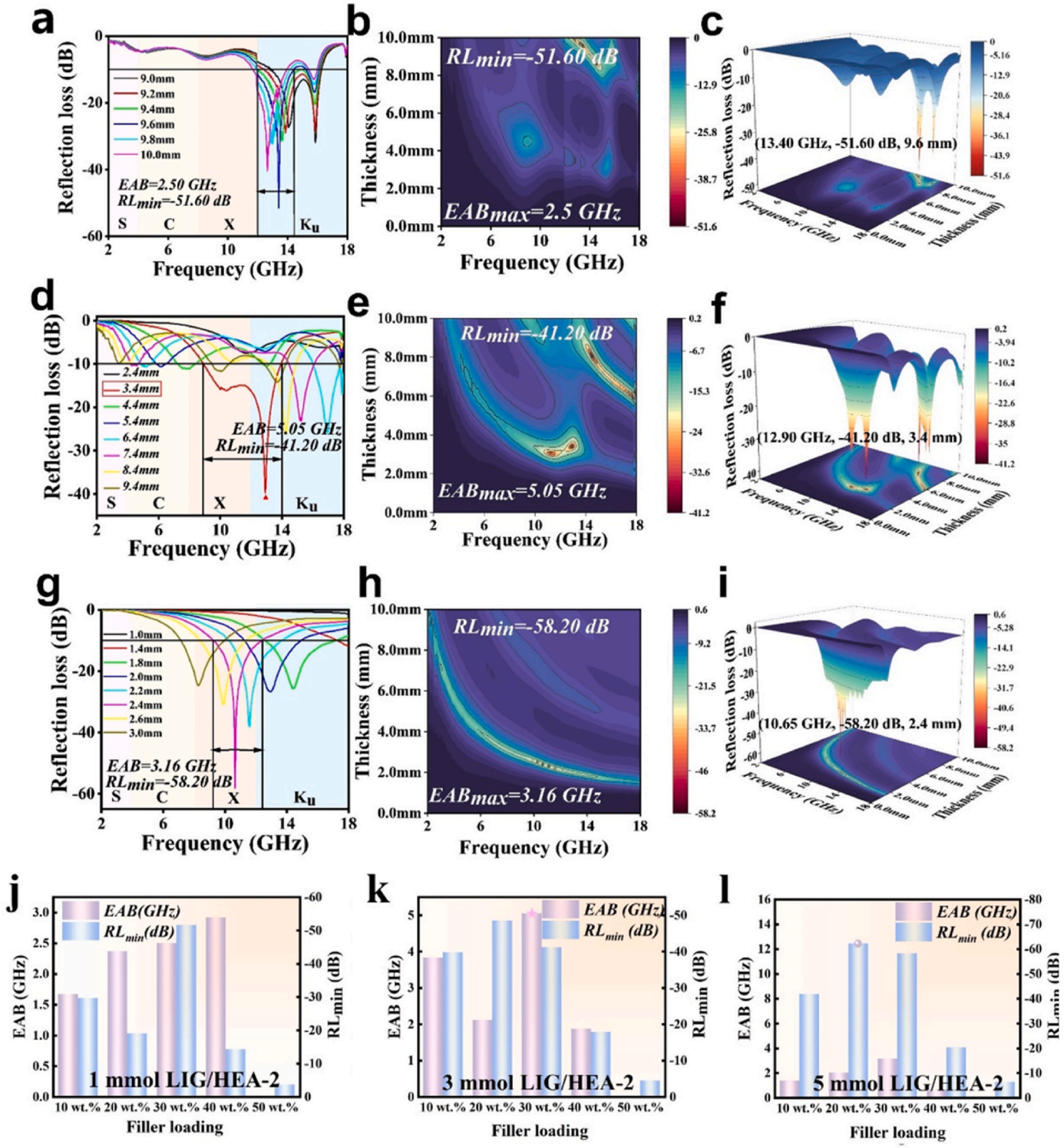

Fig. 5. Electromagnetic wave absorption properties of LIG/HEA-2 composites. (a–c) 1 mmol LIG/HEA-2, (d–f) 3 mmol LIG/HEA-2 and (g–i) 5 mmol LIG/HEA-2 with filler loadings of 30 %; (j–l) Statistical bar charts of EABw and minimum RL_{min} for LIG/HEA-2 composites with varying filler loadings and precursor concentrations.

The synergistic effects of multiple elements on M_s and Hc are common in HEAs. To further investigate the influence of Cu and Mn on magnetic properties, the hysteresis loops of LIG/HEA-1-Cu_x (x = 0.2, 0.4, 0.6, 0.8) were analyzed (Fig. 4a–b). As the proportion of Cu increases and Mn decreases, the M_s of the composites decreases, while the Hc increases. This is consistent with the formation of a FCC phase in FeCoNiCuMn alloys, indicating that Cu and Mn do not introduce significant secondary phases. This further confirms that Cu and Mn mutually regulate the overall magnetic properties of the HEAs.

In summary, the addition of Cu and Mn likely optimizes the magnetic phase distribution in FeCoNiCuMn, reducing the formation of non-magnetic or antiferromagnetic phases, thereby enhancing M_s. Cu-induced lattice distortion lowers the Hc, while the high-entropy effect and nanostructure of the alloy elements promote magnetic domain wall movement, maintaining high M_s while reducing Hc [51].

To further investigate the magnetic properties, the hysteresis loops of LIG/HEA-2 prepared with precursor salt solution concentrations of 1 mmol, 3 mmol, and 5 mmol were analyzed. As shown in Fig. 4c–d, the M_s of LIG/HEA-2 under 1 mmol precursor solution is 2.5 emu/g, with a Hc of 78 Oe. For the 3 mmol LIG/HEA-2 under 3 mmol, the M_s is 12.2 emu/g, and the Hc is 133 Oe. For the LIG/HEA-2 under 5 mmol, the M_s is 5.7 emu/g, and the coercivity is 90 Oe. The concentration of the precursor salt solution plays a crucial role in forming HEA particles. If the concentration is either too high or too low, it can lead to non-uniform distribution and agglomeration of the alloy particles. This, in turn, negatively impacts the magnetic properties of the composites. When comparing the M_s and Hc of LIG/HEA-2 with LIG/HEA-1 under 3 mmol, it was found that the M_s of LIG/HEA-2 after FJH treatment is about twice that of LIG/HEA-1. This may be due to the rapid heating and cooling process during the FJH treatment, which leads to grain refinement. Smaller grain sizes can optimize the magnetic domain structure, thereby improving the magnetization efficiency and increasing M_s [38]. However, the Hc also increases, but it still remains below 180 Oe, indicating that the material has a relatively low Hc [52]. The change in Hc of LIG/HEA-2 may be related to internal stress, as the release of internal stress during the FJH process can lead to an increase in Hc. Therefore, LIG/HEA-2 under the precursor concentration of 3 mmol exhibits superior magnetic properties (quantified in Table S1) and can effectively absorbs electromagnetic waves through magnetic loss, which will be further analyzed in the following sections.

To test the EWA performance of the composites, absorbing rings were prepared by mixing LIG/HEA composites with paraffin at mass ratios of 10 wt%, 20 wt%, 30 wt%, 40 wt%, and 50 wt% (LIG/HEA to the total mixture). These samples were tested using a vector network analyzer in the frequency range of 2–18 GHz to evaluate the reflection loss (RL_{min}) capabilities of materials with different thicknesses. When the RL_{min} value is less than −10 dB, indicating that 90 % of the incident electromagnetic waves are absorbed, the corresponding frequency range is defined as the Effective Absorption Bandwidth (EABw). Fig. 5a–c shows the 2D and 3D plots of RL_{min} versus thickness and frequency for LIG/HEA-2 composites with 1 mmol precursor concentration and a composite-to-paraffin ratio of 30:70. As can be seen, the EABw of LIG/HEA-2 is 2.50 GHz at a thickness of 9.6 mm, and the minimum RL_{min} is −51.60 dB at a frequency of 13.40 GHz. Due to the low concentration of precursor solution, the crystallinity of the HEAs is poor, and the EWA performance of the composite is reduced.

With the precursor solution concentration increases to 3 mmol, the EABw of the LIG/HEA-2 composites is 5.05 GHz (8.96 GHz–14.01 GHz) at a thickness of 3.4 mm, covering part of the X-band and Ku-band, and the minimum value of the RL_{min} reaches −41.20 dB at the frequency of 12.90 GHz; the RL_{min} is enhanced when the concentration is 5 mmol, but the EABw does not increase. As can be seen, the EABw reaches 3.16 GHz at a thickness of 2.4 mm, and the minimum RL_{min} is −58.20 dB at a frequency of 10.65 GHz, which is better than that of the 1 mmol sample but worse than that of the 3 mmol sample, indicating that excessive concentration may lead to nanoparticle aggregation, shortening the transmission path of electromagnetic waves within the composite. Concurrently, the progressive reduction in matching thickness — from 9.6 mm (1 mmol) to 2.4 mm (5 mmol) — significantly enhances practical applicability by enabling thinner absorbers. Moreover, as the concentration increases, the minimum RL_{min} shifts towards the low-frequency region, possibly due to the enhanced magnetic loss characteristics, which improves the absorption performance in the low-frequency region. Therefore, LIG/HEA-2 under precursor concentration of 3 mmol exhibits the best EWA performance. Additionally, depending on the actual needs of the absorption frequency band, different precursor concentrations can be selected to achieve matching absorption performance.

To further investigate the impact of the filler loading on the EWA performance of the composites, LIG/HEA-2 composites with precursor concentrations of 1, 3, and 5 mmol were mixed with paraffin at different mass ratios (10 wt%, 20 wt%, 40 wt%, 50 wt%). The 3D plots of RL_{min} versus frequency and thickness are shown in Fig. S7–10. The results indicate that as the filler loading of the composites increases, the EWA capability gradually weakens. This suggests that a higher filler loading may lead to a mismatch of the impedance between the surface of material and the free space, causing more electromagnetic waves to be reflected rather than absorbed.

Fig. 5j–l shows the statistical bar charts of the EABw and minimum RL_{min} for composites with filler loadings of 10 wt%-50 wt%. Among them, for the 5 mmol LIG/HEA-2 composite, when the filler ratio is 20:80 and the thickness is 7.3 mm, the EABw is 2.01 GHz, and the minimum RL_{min} reaches −62.23 dB at a frequency of 11.6 GHz, which is the best RL_{min} for all samples. Additionally, comprehensive comparisons of electromagnetic wave absorption properties are provided in Supporting Information Figs. S8 to S13.

To verify the EWA advantage of the LIG/HEA-2 composites, LIG-2 (pure graphene prepared by laser induction on PI films and subjected to the same FJH treatment parameters as LIG/HEA-2), pure HEA powders and the LIG/HEA-1 control group were tested under the conditions of a precursor concentration of 3 mmol and a filler ratio of 30:70. The results show that for LIG-2, the minimum RL_{min} is −8.74 dB at a thickness of 1.1 mm and a frequency of 17.60 GHz, with no EABw (as shown in Fig. S11). For Pure HEA powders, the EABw is 1.1 GHz at a thickness of 10.0 mm, and the minimum RL_{min} is −37.3 dB at a frequency of 17.32 GHz (as shown in Fig. S12). In contrast, the LIG/HEA-2 composites prepared after FJH treatment exhibit significantly enhanced EWA performance, demonstrating the advantage of this process.

From the above analysis, it can be observed that the LIG/HEA-2 composites exhibit outstanding EWA performance. To gain a deeper understanding of the intrinsic mechanisms, further studies were conducted on the electromagnetic parameters of the materials, including the complex permittivity (ε' and ε''), complex permeability (μ' and μ''), eddy current loss (C_0), and attenuation constant (α). The frequency dependence of the complex permittivity and complex permeability will further reveal the electromagnetic response mechanisms of the composites in different frequency bands, providing a theoretical understanding for their EWA performance.

Fig. 6a–c presents the electromagnetic parameter analysis results of 1, 3, and 5 mmol LIG/HEA-2 composites at a filler ratio of 20:80. As shown in Fig. 6a, the ε' of 5 mmol LIG/HEA-2 composite decreases more rapidly with increasing frequency compared to the 1 mmol and 3 mmol composites, indicating that the interface polarization effect is most pronounced at this precursor concentration [53]. Fig. 6a also shows that the 5 mmol LIG/HEA-2 composite exhibits the highest ε'', indicating more effective interfaces due to a higher density of nanoparticles. The ε'' peak in the 10–14 GHz range suggests uneven charge distribution at the HEA/LIG interface, causing fluctuations in ε''.

Fig. 6b shows the frequency-dependent permeability of the composites. The 5 mmol LIG/HEA-2 composite exhibits the highest permeability, indicating stronger magnetic loss and more efficient conversion of magnetic field energy into heat, likely due to a higher density of

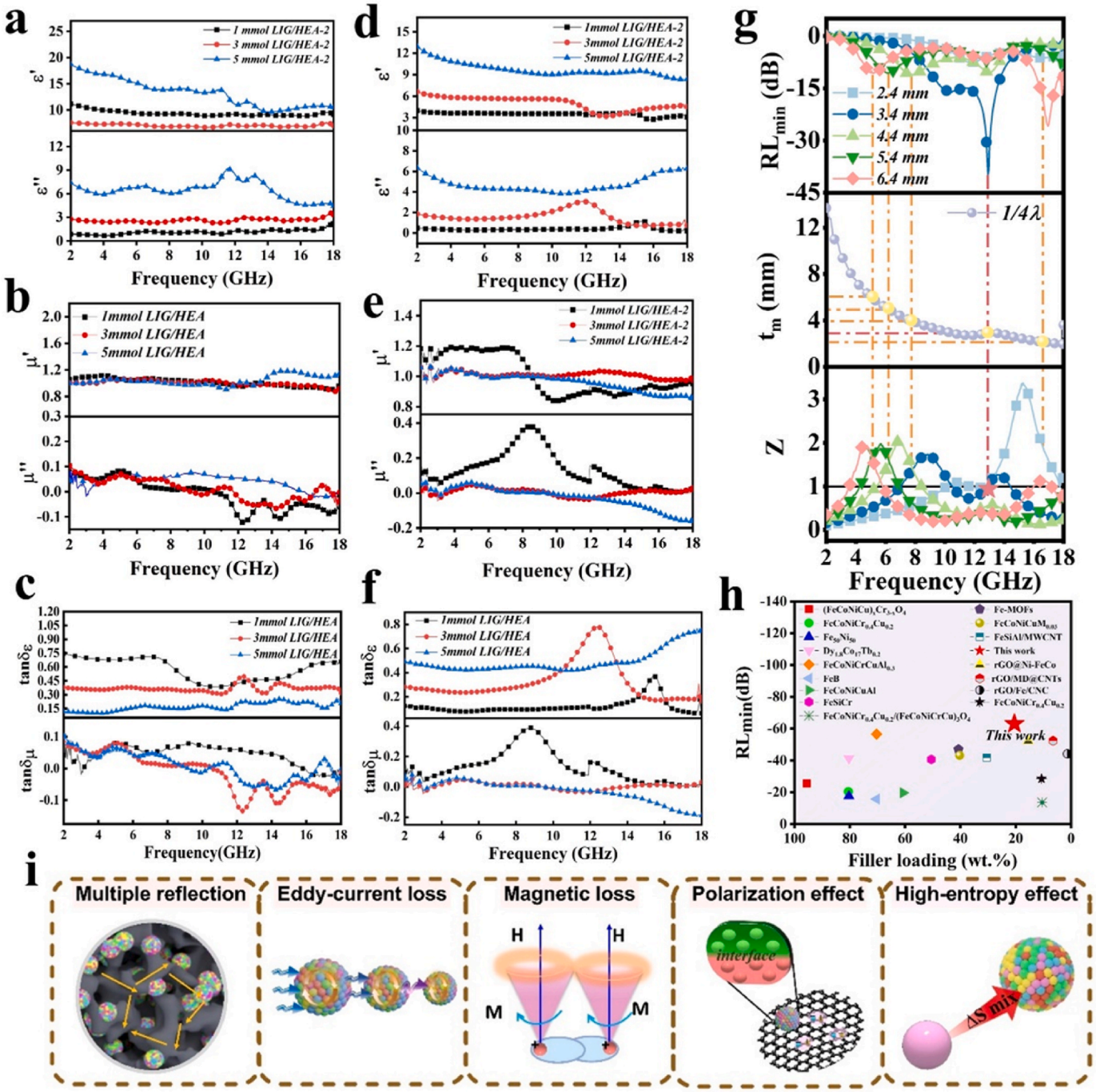

Fig. 6. Electromagnetic parameters analysis of LIG/HEA-2 materials. (a–c) Frequency dependence of ε′, ε″, μ′, μ″, and dielectric loss tangent for a 20:80 filler ratio at 1、3、5 mmol precursor concentration; (d–f) Frequency dependence of ε′, ε″, μ′, μ″, and dielectric loss tangent for a 30 wt% filler ratio at 1、3、5 mmol precursor concentration; (g) RL_{min} values of LIG/HEA-2 (30 wt%, 3 mmol) with frequency at typical thickness, showing the relationship between thickness and frequency in λ/4 theory and the input impedance ($|Z_{in}/Z_0|$); (h) Comparison of EM wave absorption performances of similar HEAs; (i) Schematic illustration of the microwave absorption mechanism of the LIG/HEA-2 composite material.

nanoparticles. As shown in Fig. 6b, the imaginary part of the permeability (μ″) fluctuates significantly in the high-frequency region and generally decreases, indicating that the magnetic loss of LIG/HEA-2 is mainly due to multiple magnetic resonances, including natural and exchange resonances. In magnetic and non-magnetic elements, the presence of certain defects can trigger magnetic ordering, thereby generating magnetism [54]. Defects between Cu and the other four magnetic elements (Fe, Co, Ni, and Mn) in HEAs may also lead to the generation of magnetism and thus magnetic loss.

Fig. 6c shows the tangent plots of the dielectric constant and permeability for 1, 3, and 5 mmol LIG/HEA-2. As the concentration of precursor salt solution increases, the tangent value of the dielectric constant tends to increase, indicating that the effect of polarization at the interface of the composite material is more significant with the increase in concentration. Meanwhile, the 3D porous graphene forms more conductive pathways, leading to increased dielectric loss. In contrast, for 1 and 3 mmol LIG/HEA-2 at a filler ratio of 20:80, the HEA particles are less dispersed in the 3D porous graphene, resulting in insufficient interfacial polarization and lower electrical conductivity and polarization loss. At low concentrations, the nanoparticles are more

dispersed, making the domain wall resonance effect weaker. Therefore, under the synergistic effect of dielectric and magnetic losses, 5 mmol LIG/HEA-2 achieves a minimum reflection loss of −62.23 dB at a filler ratio of 20:80, realizing effective absorption of electromagnetic waves.

Fig. 6d–f shows the electromagnetic parameter analysis results of 1, 3, and 5 mmol LIG/HEA-2 at a filler ratio of 30:70. Fig. 6d shows the frequency dependence of the real (ε') and imaginary (ε'') parts of the complex dielectric constant. ε' decreases with frequency, with the 5 mmol LIG/HEA-2 composite exhibiting the highest ε', followed by the 3 mmol and 1 mmol composites. Notably, the ε' of 5 mmol LIG/HEA-2 at a filler ratio of 30:70 is approximately 12, significantly lower than its value of around 22 at a filler ratio of 20:80, indicating reduced conductive loss and consistent with its lower RL_{min} (−58.20 dB) at the 30:70 filler ratio. Importantly, grain refinement drastically enhances dielectric loss properties. This is evidenced by LIG/HEA-2 exhibiting a 7-fold higher imaginary permittivity (ε'') at 2 GHz and a surge in dominant polarization loss (0.38 → 2.07 at 10 GHz) compared to LIG/HEA-1, resulting from amplified interfacial polarization and Maxwell-Wagner effects at the increased density of heterogeneous interfaces.

Fig. 6e shows the frequency dependence of the real (μ') and imaginary (μ'') parts of the complex permeability for 1 mmol, 3 mmol, and 5 mmol LIG/HEA-2 composites. The permeability remains relatively stable. At a filler ratio of 30:70, the μ'' of 1 mmol LIG/HEA-2 is higher than that at a filler ratio of 20:80, indicating that the composite with a higher filler loading and a larger number of magnetic nanoparticles significantly enhances magnetic loss and electromagnetic wave absorption.

Fig. 6f presents the frequency dependence of the dielectric and permeability tangents for 1 mmol, 3 mmol, and 5 mmol LIG/HEA-2 composites. The results further demonstrate that the synergistic effect of dielectric and magnetic losses significantly enhances electromagnetic wave absorption efficiency. Overall, the frequency-dependent electromagnetic parameters highlight the material's ability to effectively absorb electromagnetic waves, with the synergistic effects of dielectric and magnetic properties playing a crucial role in improving absorption performance.

Fig. 6g shows the results for a filler ratio of 30:70, where the optimal thickness of 3 mmol LIG/HEA-2 is determined using the $\lambda/4$ theory and impedance matching. The results indicate that the RL_{min} reaches its minimum value at a thickness of 3.4 mm, which also meets the $\lambda/4$ matching condition. This suggests that the electromagnetic waves can enter the material to the greatest extent and be absorbed. The EABw is 5.05 GHz, and the input impedance ($|Z_{in}/Z_0|$) is close to 1, indicating good impedance matching characteristics. These findings demonstrate the superior EWA performance of 3 mmol LIG/HEA-2, highlighting its potential for practical applications.

Fig. 6h compares this work with other studies [12,13,15,16,21–23,25,52,55–61], demonstrating superior electromagnetic wave absorption (EWA) performance under low loading conditions.

The exceptional electromagnetic wave absorption performance of the LIG/HEA-2 composites originates from synergistic optimization of impedance matching and multi-scale loss mechanisms, as comprehensively validated through advanced characterization techniques. Building on detailed analysis of complex permittivity (ε', ε'') and permeability (μ', μ'') [62–64], we gain critical insights via Cole-Cole semicircle analysis (Fig. S13) [65], eddy current loss quantification (Fig. S14) [66], and attenuation constant calculations [67]. These analyses demonstrate that optimized polarization behavior and dual magnetic-dielectric synergism significantly enhance absorption, particularly at 30 wt% filler ratios with 3 mmol precursor concentration. Systematic impedance matching analysis confirms near-perfect matching ($|Z_{in}/Z_0|\approx1$ at 11.60 GHz) enables >99 % wave penetration, underpinning the record −62.23 dB reflection loss at 20 wt% loading. The permittivity-driven mechanism features pronounced interfacial polarization at graphene/HEA interfaces (characteristic 12–14 GHz peak in Fig. S13), with dielectric loss decomposition (Fig. S16) confirming polarization dominance over conductive loss. Complementarily, permeability analysis reveals frequency-dependent magnetic dissipation: natural resonance dominates <6 GHz ($C_0 \approx 0$ in Fig. S14a) while the characteristic peaks >6 GHz are dominated by exchange resonance (increasing C_0). This multi-scale synergy - integrating interfacial polarization, dual-phase magnetic loss, and optimized impedance - achieves maximum bandwidth (EAB = 5.05 GHz) at 30 wt% loading, as visually synthesized in the attenuation mechanism schematic (Fig. 6i).

In practical engineering applications, the radar cross section (RCS) can reflect the true far-field conditions of electromagnetic waves [67]. To evaluate the EWA characteristics of the composites, the RCS simulation analysis of LIG/HEA-2 was carried out by considering the response performance of experimental parameters to electromagnetic waves. Fig. 7 presents the simulation results. The model consists of an absorber and a perfect electric conductor (PEC). The electromagnetic wave incidence simulation model is shown in Fig. 7a. In the RCS simulation, the positive x-axis and Phi represent the incident direction and the detection angle, respectively. Fig. 7b and g presents the angular-dependent RCS performance of LIG/HEA-2 composites with 20 wt% and 30 wt% filler loadings, respectively. For 20 wt% composites (Fig. 7b), all samples (1–5 mmol) maintain RCS values below −10.0 dB m^2 across 0–180°. The RCS reduction (ΔRCS=PEC-absorber) at 90° increases progressively from 9.83 dB m^2 (1 mmol) to 19.84 dB m^2 (3 mmol), reaching 28.0 dB m^2 (5 mmol), demonstrating concentration-dependent enhancement. Interestingly, 30 wt% composites (Fig. 7e) show non-monotonic behavior: ΔRCS first decreases from 17.34 dB m^2 (1 mmol) to 9.29 dB m^2 (3 mmol), then rebounds to 21.39 dB m^2 (5 mmol), suggesting optimal HEA loading varies with precursor concentration. These trends highlight the complex interplay between filler content and metal ion concentration in electromagnetic attenuation. The 3D distribution of RCS was further presented to represent the radar wave scattering signal. When the filler ratio is 30 wt% for 3 mmol LIG/HEA-2 and 20 wt% for 5 mmol LIG/HEA-2, the vertical reflection intensity (Fig. 7c1 and 7d1) is lower than that of the PEC plate (Fig. 7c2 and 7d2), indicating that these composites have a strong ability to effectively attenuate electromagnetic waves. Additionally, the 2D bistatic scattering RCS diagrams (Fig. 7f and g) show that after applying the absorber coating to the PEC plate, the RCS area decreases, indicating that this absorber coating has broad application prospects for electromagnetic wave attenuation under conditions of large grazing angle incidence. These results demonstrate the significant potential of LIG/HEA-2 for practical applications in electromagnetic wave absorption.

4. Conclusion

This study demonstrates the in-situ synthesis of 3D graphene/HEA composites using a novel method that combines laser-induced synthesis and flash Joule heating (FJH), resulting in significantly enhanced electromagnetic wave absorption performance. The synergistic effect of the FeCoNiCuMn HEA composition, where the five elements work together, optimizes the magnetic and dielectric properties of the composites. Specifically, the FJH process refines the grain size of the alloy, which significantly improves impedance matching and increases the saturation magnetization while reducing the coercivity. Additionally, the 3D porous graphene structure provides a lightweight and conductive matrix, promoting multiple reflections and scattering of electromagnetic waves. As a result, the composites achieve a minimum reflection loss of −62.23 dB at 2–18 GHz with a filler ratio of 20 wt% in paraffin wax and an effective absorption bandwidth of 5.05 GHz with a filler ratio of 30 wt %. These findings highlight the potential of 3D graphene/HEA composites synthesized via laser-induced and FJH methods for advanced electromagnetic wave absorbing materials, with broad applications in electromagnetic compatibility, stealth technology, and communication systems.

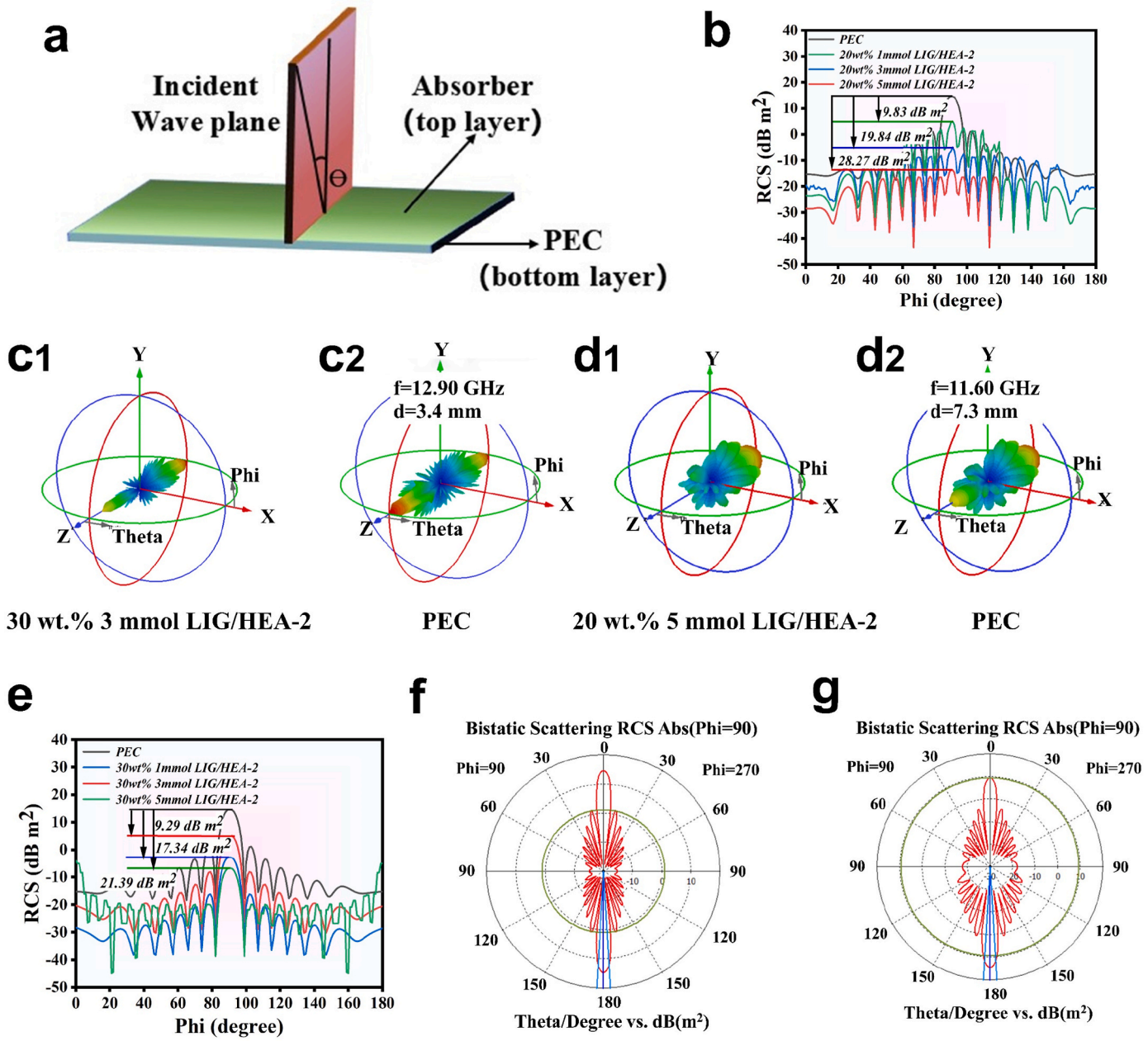

Fig. 7. Radar cross-section (RCS) simulation of composites based on real conditions. (a) Modeling of composite-coated PEC plate. (b) RCS curve for 20 wt%, 1、3、5 mmol LIG/HEA-2; (c1-d2) 3D radar scattering results for 30 wt%, 3 mmol LIG/HEA-2, PEC, 20 wt%, 5 mmol LIG/HEA-2 and PEC; (e) RCS curve for 30 wt%,1、3、5 mmol LIG/HEA-2; (f–g) 2D radar scattering results for 30 wt%, 3 mmol LIG/HEA-2 and PEC plates.

CRediT authorship contribution statement

Wen Fan: Software, Writing – original draft, Formal analysis, Writing – review & editing, Methodology, Data curation. **Zhao Li:** Supervision, Validation. **Jixiang Zhang:** Supervision. **Yanping Song:** Conceptualization. **Shudong Zhang:** Conceptualization. **Cui Liu:** Conceptualization. **Shuai Han:** Conceptualization. **Yi Dong:** Conceptualization. **Zheng Xu:** Conceptualization. **Na Hong:** Conceptualization. **Jun Kang:** Conceptualization. **Shihao Wang:** Conceptualization. **Zhiyuan Yang:** Software. **Nian Li:** Resources, Supervision. **Zhenyang Wang:** Conceptualization.

Declaration of competing interest

The authors declare that they have no known competing financial interests or personal relationships that could have appeared to influence the work reported in this paper.

Acknowledgement

This work was supported by the National Key Research and Development Project (Grant No. 2020YFA0210703, 2022YFA1203604), the National Natural Science Foundation of China (Grants Nos. 52171053 and 12204488), CAS Project for Young Scientists in Basic Research (Grant No.YSBR-070), the HFIPS Director's Fund (Grant No. YZJJ-GGZX-2022-01 and GGZX-GTCX-2023-01), the Science Research Project of Hebei Education Department (QN2024232), the Natural Science Foundation of Hebei Province (E2024402130), Science Research Project of Hebei Education Department (QN2024232). Joint Training Base Construction Project for Graduate Students in Chongqing

(JDLHPYJD2020031).Shandong Province Science and Technology Small and Medium-sized Enterprise Innovation Ability Promotion Project (2024TSGC0948).

Appendix A. Supplementary data

Supplementary data to this article can be found online at https://doi.org/10.1016/j.carbon.2025.120561.

References

[1] X.J. Zeng, X.Y. Cheng, R.H. Yu, D. Galen, Stucky, electromagnetic microwave absorption theory and recent achievements in microwave absorbers, Carbon (2020) 606–623.

[2] H.H. Chen, Wenle Ma, Z.Y. Huang, Y. Zhang, Y. Huang, Y.S. Chen, Graphene-based materials toward microwave and terahertz absorbing stealth technologies, Adv. Opt. Mater. (2019) 1801318.

[3] D. Lan, Y. Hu, M. Wang, Y. Wang, Z.G. Gao, Z.R. Ji, Perspective of electromagnetic wave absorbing materials with continuously tunable effective absorption frequency bands, Compos. Commun. (2024) 101993.

[4] J.Y. Cheng, H.B. Zhang, M.Q. Ning, H. Raza, D.Q. Zhang, G.P. Zheng, et al., Emerging materials and designs for low-and multi-band electromagnetic wave absorbers: the search for dielectric and magnetic synergy? Adv. Funct. Mater. 32 (23) (2022) 2200123.

[5] J.W. Ding, R.R. Shi, C.C. Gong, C.X. Wang, Y. Guo, Tchen, et al., Defect engineering activates schottky heterointerfaces of graphene/$CoSe_2$ composites with ultrathin and lightweight design strategies to boost electromagnetic wave absorption, Adv. Funct. Mater. 33 (48) (2023) 2305463.

[6] S.K. Hou, Y. Wang, F. Gao, H. Yang, F. Jin, L. Ren, , et al.Wang, A novel approach to electromagnetic wave absorbing material design: utilizing nano-antenna arrays for efficient electromagnetic wave capture, Chem. Eng. J. 471 (2023) 144779.

[7] T.B. Zhao, T.T. Zheng, D. Lan, Y. Zhang, Z.S. Sun, C. Wang, et al., Self-assembly tungsten selenide hybrid ternary MOF derived magnetic alloys via multi-polarization to boost microwave absorption, Nano Res. 17 (3) (2024) 1625–1635.

[8] X.Y. Liu, S.Y. Xie, X.Y. Liu, Z.J. Yu, S.Y. Cai, G.X. Tong, et al., Heterointerface-engineered SnO_2@ SnO nanoparticle@ foamed C composites for prominent microwave absorption and thermal conduction performance, Chem. Eng. J. 497 (2024) 154492.

[9] C.H. Wang, Y.N. Zhang, W.A. Kong, Nickel sulfide/graphene composites for electromagnetic wave absorption, ACS Appl. Nano Mater. (2024) 27124–27133.

[10] Z.C. Wu, H.W. Cheng, C. Jin, B.T. Yang, C.Y. Xu, K. Pei, et al., Dimensional design and core–shell engineering of nanomaterials for electromagnetic wave absorption, Adv. Mater. 34 (2022) 2107538.

[11] L.Y. Li, M. Zhang, M. Jiang, L.H. Gao, Z. Ma, M.S. Cao, High entropy ceramics for electromagnetic functional materials, Adv. Funct. Mater. (2024) 2416673.

[12] X.J. Liu, Y.P. Duan, Y. Guo, H.F. Pang, Z.R. Li, X.Y. Sun, T.M. Wang, Microstructure design of high-entropy alloys through a multistage mechanical alloying strategy for temperature-stable megahertz electromagnetic absorption, Nano-Micro Lett. 14 (1) (2022) 142.

[13] X.J. Liu, Y.P. Duan, Y. Guo, Z. Li, J.B. Ma, J.R. Di, T.M. Wang, In situ construction of complex spinel ferrimagnet in multi-elemental alloy for modulating natural resonance and highly efficient electromagnetic absorption, Chem. Eng. J. 462 (2023) 142200.

[14] S.F. Gang, H. He, H. Long, Y.C. Wei, W.G. Zhang, X. Li, et al., 2D-High entropy alloys embedded in 3D-Carbon foam towards light-weight electromagnetic wave absorption and hydrophobic, Thermal Insulation. Nano Energy. (2025) 110642.

[15] Y. Guo, Y.P. Duan, S. Gu, X.J. Liu, Z. Fan, H.F. Pang, L.J. Pan, Carbon nanocoils-assisted formation of tunable pore graphene aerogels for lightweight broadband microwave absorption, thermal insulation, and antifreeze devices, Small (2025) 2412270.

[16] Y. Guo, Y.P. Duan, X.J. Liu, H. Zhang, T.K. Yuan, N.X. Wen, C.W. Li, H.F. Pang, et al., Boosting conductive loss and magnetic coupling based on "size modulation engineering" toward lower-frequency microwave absorption, Small 20 (17) (2024) 2308809.

[17] Y.P. Duan, M.M. Gao, H.F. Pang, T.M. Wang, FeCoNiMnAl high-entropy alloy: improving electromagnetic wave absorption properties, J. Mater. Res. (2021) 2107–2117.

[18] L. Jia, L.W. Jiang, J.P. Yang, J.Y. Liu, A.H. Wu, X.F. Zhang, Tunable electromagnetic properties via dealloying in FeCoNiCuAl high-entropy alloys for efficient electromagnetic-wave absorption, Appl. Phys. Lett. 124 (2024) 9.

[19] H.R. Zhou, L.W. Jiang, L. Jia, Z. Tang, L.L. Wang, A.H. Wu, et al., Ultrawide-frequency electromagnetic-wave absorption based on $FeCoNiCu_xMn$ high entropy alloys synthesized through swing ball-milling, J. Mater. Chem. C 10 (44) (2022) 16696–16705.

[20] X.J. Liu, Y.P. Duan, N. Wu, G.M. Li, Y. Guo, J.Y. Liu, N. Zhu, Q. Wang, L. Wang, Z. C. Xu, et al., Modulating electromagnetic genes through Bi-phase high-entropy engineering toward temperature-stable ultra-broadband megahertz electromagnetic wave absorption, Nano-Micro Lett. 17 (1) (2025) 1–16.

[21] Z.G. Qiu, X.Y. Liu, T.Y. Yang, J.B. Wang, Y. Wang, W. Ma, et al., Synergistic enhancement of electromagnetic wave absorption and corrosion resistance properties of high entropy alloy through lattice distortion engineering, Adv. Funct. Mater. (2024) 2400220.

[22] Y. Guo, Y.P. Duan, X.J. Liu, J. Tian, N.X. Wen, Z. Fan, L.J. Pan, Construction of rGO/MOF-derived CNTs aerogel with multiple losses for multi-functional efficient electromagnetic wave absorber, Carbon 230 (2024) 119591.

[23] Y. Guo, Y.P. Duan, X.J. Liu, Y.P. Shi, Z. Fan, H.F. Pang, L.J. Pan, Construction of multiple heterogeneous interfaces induced by rGO-multimetallic LDH derivatives to improve dielectric loss for enhanced electromagnetic wave absorption, J. Mater. Sci. Technol. 237 (2025) 288–297.

[24] X.J. Liu, Y.P. Duan, X. Yang, L.X. Huang, M.M. Gao, T.M. Wang, Enhancement of magnetic properties in $FeCoNiCr_{0.4}Cu_X$ high entropy alloys through the cocktail effect for megahertz electromagnetic wave absorption, J. Alloys Compd. 872 (2021) 159602.

[25] X. Liu, Y. Duan, Z. Li, H.F. Pang, L.X. Huang, et al., $FeCoNiCr_{0.4}Cu_X$ High-entropy alloys with strong intergranular magnetic coupling for stable megahertz electromagnetic absorption in a wide temperature spectrum, ACS Appl. Mater. Interfaces 14 (5) (2022) 7012–7021.

[26] G.H. Fan, X.T. Song, X.P. Zhang, Q.Y. Wang, Y.N. Tang, Y. Liu, Biomass-derived ferrous magnetic carbon-based nanocomposites from loofah collaterals for excellent electromagnetic wave-absorbing materials, J. Alloys Compd. 969 (2023) 172384.

[27] Y.H. Lu, S.L. Zhang, M.Y. He, L. Wei, Y. Chen, R.N. Liu, 3D cross-linked graphene Or/And MXene based nanomaterials for electromagnetic wave absorbing and shielding, Carbon (2021) 413–435.

[28] Y.X. Li, Y.J. Liao, L.Z. Ji, C.L. Hu, Z.H. Zhang, Z.Y. Zhang, et al., Quinary high-entropy-alloy@ graphite nanocapsules with tunable interfacial impedance matching for optimizing microwave absorption, Small (2022) 2107265.

[29] F.H. Mohammadabadi, S.M. Masoudpanah, S. Alamolhoda, Electromagnetic microwave absorption properties of high entropy spinel ferrite $((MnNiCuZn)_{1-x}Co_xFe_2O_4)$/graphene nanocomposites, J. Mater. Res. Technol. 14 (2021) 1099–1111.

[30] M.Y. Rekha, N. Mallik, C. Srivastava, First report on high entropy alloy nanoparticle decorated graphene, Sci. Rep. (2018) 8737.

[31] Y.P. Song, N. Li, S. Han, S.D. Zhang, L.Q. Chen, Z. Li, et al., Macro-sized all-graphene 3D structures via layer-By-layer covalent growth for micro-to-macro inheritable electrical performances, Adv. Funct. Mater. (2023) 2305191.

[32] X.L. Yu, N. Li, S.D. Zhang, C. Liu, L.Q. Chen, Y.P. Song, , et al.Wang, Enhancing the energy storage capacity of graphene supercapacitors via solar heating, J. Mater. Chem. A 10 (7) (2022) 3382–3392.

[33] R.q. Ye, Z.W. Peng, T. Wang, Y.N. Xu, J.B. Zhang, Y.L. Li, et al., In situ formation of metal oxide nanocrystals embedded in laser-induced graphene, ACS Nano 9 (9) (2015) 9244–9251.

[34] L. Cheng, C.S. Yeung, L.B. Huang, G. Ye, J. Yan, W.P. Li, et al., Flash healing of laser-induced graphene, Nat. Commun. 15 (1) (2024) 2925.

[35] J. Yin, J.X. Zhang, S.D. Zhang, C. Liu, X.L. Yu, L.Q. Chen, et al., Flexible 3D porous graphene film decorated with nickel nanoparticles for absorption-dominated electromagnetic interference shielding, Chem. Eng. J. 421 (2021) 129763.

[36] H.Q. Jiang, X.T. Liu, M.N. Zhu, J. Xu, L.C. An, P.F. Sui, et al., Nanoalloy libraries from laser-induced thermionic emission reduction, Sci. Adv. 8 (16) (2022) eabm 6541.

[37] J.Y. Lv, T. Li, Y. Li, H. Li, Z.W. Xia, S.W. Zhang, et al., Laser-induced self-propagating synthesis of Al_3BC_3 powder for high-temperature electromagnetic wave absorption, J. Am. Ceram. Soc. (2024) e20306.

[38] Y.M. Li, Y.R. Li, H.P. Fang, Y. Deng, D.Y. Wang, Optimization design of the multidimensional heterostructure toward lightweight, broadband, highly efficient, and flame-retarding electromagnetic wave-absorbing composites, ACS Appl. Mater. Interfaces 16 (38) (2024) 51333–51345.

[39] B. Deng, L. E, K. W, C.S. T, J.M. T, Flash joule heating for synthesis, upcycling and remediation, Nat. Rev. Clean Tech. 1 (1) (2025) 32–54.

[40] J.H. Cha, S.H. Cho, D.H. Kim, D. J, S. P, et al., Flash-thermal shock synthesis of high-entropy alloys toward high-performance water splitting, Adv. Mater. 35 (46) (2023) 2305222.

[41] J. Ahn, S. Park, D.H. Oh, Y.S. Lim, J.S. Nam, J. Kim, et al., Rapid Joule heating synthesis of oxide-socketed high-entropy alloy nanoparticles as CO_2 conversion catalysts, ACS Nano 17 (13) (2023) 12188–12199.

[42] L. Eddy, S.C. Xu, C.H. Liu, P. Scotland, W.Y. Chen, J.L. Beckham, et al., Electric field effects in flash Joule heating synthesis, J. Am. Chem. Soc. 146 (2024) 16010–16019.

[43] Y.T. Liao, R.T. Zhu, W.J. Zhang, H.Y. Zhu, Y. Sun, J. Chen, et al., Transient synthesis of carbon-supported high-entropy alloy sulfide nanoparticles via flash Joule heating for efficient electrocatalytic hydrogen evolution, Nano Res. 17 (4) (2024) 3379–3389.

[44] S.P. Wang, Q.C. Liu, S.K. Li, F.Z. Huang, H. Zhang, Joule-heating-driven synthesis of a honeycomb-like porous carbon nanofiber/high entropy alloy composite as an ultralightweight electromagnetic wave absorber, ACS Nano 18 (6) (2024) 5040–5050.

[45] J.J. Liang, G.H. Cao, M.Q. Zeng, L. Fu, Controllable synthesis of high-entropy alloys, Chem. Soc. Rev. 53 (2024) 6021–6041.

[46] Y.P. Duan, H.F. Pang, X. Wen, X.F. Zhang, T.M. Wang, Microwave absorption performance of $FeCoNiAlCr_{0.9}$ alloy powders by adjusting the amount of process control agent, J. Mater. Sci. Technol. 77 (2021) 209–216.

[47] L. Cheng, C.S. Yeung, L.B. Huang, G. Yan, W.P. Li, C.K. Yiu, et al., Flash healing of laser-induced graphene, Nat. Commun. 15 (1) (2024) 2925.

[48] Y.Z. Zhang, Y.D. Chen, Q.D. Qin, W. Li, Synthesis of FeCoNiCuZn single-phase high-entropy alloy by high-frequency electromagnetic-field assisted ball milling, J. Magn. Magn Mater. 498 (2020) 166151.

[49] Z.Y. Ji, Q. Wang, Z.H. Wang, Y.P. Duan, C. Dong, P.K. Liaw, Electromagnetic wave-absorbing behavior of soft-magnetic medium entropy alloys with BCC/$L2_1$ coherent microstructure, Mater. Des. 222 (2022) 111054.
[50] J.W. Hu, L.W. Jiang, L. Jia, J.W. Jin, A.H. Wu, X.F. Zhang, Novel carbonitriding process of high-entropy alloys using mechanochemical process for obtaining excellent high-frequency electromagnetic properties, Carbon 228 (2024) 119406.
[51] H.G. Zhang, P.L. Chen, B.T. Song, Y.Q. Li, X.M. Zhang, W.Q. Liu, et al., Enhancing ferromagnetism in the Sm $(Co, Mn)_5$ system: impact on phase stability and magnetic properties, Mater. Today Phys. 44 (2024) 101446.
[52] D. Lan, Z.H. Zhao, Z.G. Gao, K.C. Kou, G.L. Wu, H.J. Wu, Porous high entropy alloys for electromagnetic wave absorption, J. Magn. Magn Mater. 512 (2020) 167065.
[53] Z. Zhao, B.H. Yao, Y.Y. Gong, Z.L. Gui, J. Wang, Effect of grain motion and Joule heat on grain refinement under a pulsed magnetic field, Mater. Today Commun. 39 (2024) 108988.
[54] X.C. Du, L.R. Zhang, C.J. Guo, G.Q. Liu, H.F. Yuan, Y. Li, et al., FeCo/Graphene nanocomposites for applications as electromagnetic wave-absorbing materials, ACS Appl. Nano Mater. 5 (12) (2022) 18730–18741.
[55] S. Isogami, Y. Kota, H. Yasufuku, K. Oyoshi, M. Tanaka, Y.K. Takahashi, Carbon-induced magnetic properties and anomalous Hall effect in Co_2Mn_2C thin films with $L1_0$-like structures, Phys. Rev. Mater. 7 (1) (2023) 014411.
[56] D.L. Tan, Q. Wang, M. Li, L.M. Song, F. Zhang, Z.Y. Min, et al., Magnetic media synergistic carbon fiber@ Ni/NiO composites for high-efficiency electromagnetic wave absorption, Chem. Eng. J. 492 (2024) 152245.
[57] L.N. Huang, X.F. Liu, D. Chuai, Y.X. Chen, R.H. Yu, Flaky FeSiAl alloy-carbon nanotubecomposite with tunable electromagnetic properties for microwave absorption, Sci. Rep. 6 (1) (2016) 35377.
[58] J.Q. Zhong, S. Liang, Y. Chen, J.J. Tan, Transient analysis of power loss density with time-harmonic electromagnetic waves in debye media, R. Soc. Open Sci. 8 (11) (2021) 210023.
[59] D. Lan, Z.H. Zhao, Z.G. Gao, K.C. Kou, G.L. Wu, H.J. Wu, Porous high entropy alloys forelectromagnetic wave absorption, J. Magn. Magn Mater. 512 (2020) 167065.
[60] Y. Chen, L. Wang, H.D. Xiong, S.U. Rehman, Q.L. Tan, Q.F. Huang, et al., Optimizedabsorption performance of FeSiCr nanoparticles by changing the shape anisotropy, Phys. Status Solidi 217 (23) (2020) 2000389.
[61] Y.P. Duan, Y.L. Cui, B. Zhang, G.J. Ma, T.M. Wang, A novel microwave absorber of FeCoNiCuAl high-entropy alloy powders: adjusting electromagnetic performance by ball milling time and annealing, J. Alloys Compd. 773 (2019) 194–201.
[62] H. Zhao, Z.H. Zhu, C. Xiong, X. Xu, Q.Y. Lin, The effect of transverse magnetic field treatment on wave-absorbing properties of FeNi alloy powders, J. Magn. Magn Mater. 422 (2017) 402–406.
[63] Z.X. Xu, T.R. Xia, L.C. Chen, R. Xiang, Q.R. Yao, Q.X. Long, et al., Effect of Tb doping amount on microwave absorption performance of Dy_2Co_{17} alloys, J. Electron. Mater. 52 (5) (2023) 3132–3145.
[64] Q. Su, D.D. Liu, C.Y. Wang, L. Xia, X.X. Huang, B. Zhong, Graphene/BN/Fe/BN nanocomposites for highly efficient electromagnetic wave absorption, ACS Appl. Nano Mater. 5 (10) (2022) 15902–15913.
[65] L. Jia, L.W. Jiang, H. Zhou, S. Yan, A.H. Wu, X.F. Zhang, Multifunctional amorphous $FeCoNiTi_xSi$ high-entropy alloys with excellent electromagnetic-wave absorption performances, Phys. Chem. Chem. Phys. 25 (33) (2023) 22011–22021.
[66] Y.L. Wang, S.H. Yang, H.Y. Wang, G.S. Wang, X.B. Sun, P.G. Yin, Hollow porous CoNi/C composite nanomaterials derived from MOFs for efficient and lightweight electromagnetic wave absorber, Carbon 167 (2020) 485–494.
[67] X.Y. Liu, S.Y. Xie, X.Y. Liu, Z.J. Yu, S.Y. Cai, G.X. Tong, et al., Heterointerface-engineered SnO_2@ SnO nanoparticle@ foamed C composites for prominent microwave absorption and thermal conduction performance, Chem. Eng. J. 497 (2024) 154492.